

Prussian Blue Analogues Derived $\text{CuO@Co}_3\text{O}_4$ Nanoparticles As Effective Oxygen Reduction Reaction Catalyst For Magnesium-Air Battery

Xiaoyang Dong

Chongqing University

Jinxing Wang (✉ wjx@cqu.edu.cn)

Chongqing University of Materials Science and Engineering College <https://orcid.org/0000-0003-4232-6773>

Xiao Wang

Chongqing University

Jingdong Yang

Chongqing University

Ling Zhu

Chongqing College of Mobile Communication

Wen Zeng

Chongqing University

Jingfeng Wang

Chongqing University

Fusheng Pan

Chongqing University

Research Article

Keywords: $\text{CuO@Co}_3\text{O}_4$, Prussian blue analogues, ORR catalyst, Mg-air battery

Posted Date: November 4th, 2021

DOI: <https://doi.org/10.21203/rs.3.rs-1023610/v1>

License:   This work is licensed under a Creative Commons Attribution 4.0 International License.

[Read Full License](#)

Version of Record: A version of this preprint was published at Journal of The Electrochemical Society on January 13th, 2022. See the published version at <https://doi.org/10.1149/1945-7111/ac4b25>.

Abstract

Developing efficient, durable and cost-effective non-noble metal catalysts for oxygen reduction reaction (ORR) is remarkably significant to promote the efficiency and performance of Mg-air battery. Herein, the $\text{CuO@Co}_3\text{O}_4$ nanoparticles are synthesized by a low-cost and simple approach using the CuCo-based prussian blue analogues (PBA) as precursor of pyrolysis at different calcination temperatures. It is found that the $\text{CuO@Co}_3\text{O}_4$ nanoparticles calcined at 600 °C (CCO-600) have relatively small size and superior ORR performance. The onset potential is 0.889 V and the diffusion limiting current density achieves $6.746 \text{ mA}\cdot\text{cm}^{-2}$, as well as prominent stability in 0.1 M KOH electrolyte. The electron transfer number of the CCO-600 is 3.89 under alkaline medium, which manifests that the reaction mechanism of ORR is dominated by 4 e process. It is similar to the commercial Pt. Moreover, the primary Mg-air battery with the CCO-600 as the cathode catalyst has been assembled. The Mg-air battery of the CCO-600 as the cathode catalyst possesses better discharge performance than the CuCo-based PBA. The open circuit voltage of CCO-600 arrives 1.76 V and energy density of 1895.95 mWh/g. This work provides an effective strategy to develop non-noble metal ORR catalyst for the application of metal-air batteries.

1 Introduction

Metal-air batteries are considered to be one of the most promising next-generation electrochemical energy conversion systems owing to high energy density, low cost, natural abundance, intrinsic safety and environmental friendliness [1–3]. Generally speaking, metal-air batteries are consisted of air cathode, electrolyte and metal anode. According to different metal anodes, they are divided into Lithium (Li)-air, Zinc (Zn)-air, Aluminum (Al)-air, Magnesium (Mg)-air battery and so on [4–7]. Among those metal-air batteries, Mg-air battery has obtained increasing attention in recent years, which attributes to the high theoretical voltage, superior energy density, low cost, abundant reserves, greater safety and good environmental compatibility [8–13]. However, the poor kinetic properties of oxygen reduction reaction (ORR) in the air cathode leads to the low coulombic efficiency and high polarization, which has seriously hindered the development and widespread application of Mg-air batteries [9, 14]. To address the issue of sluggish kinetic in air cathode, it is very essential to develop efficient and suitable ORR catalysts, which can accelerate reaction rate and enhance energy conversion efficiency of Mg-air batteries [15–17]. Traditional noble-metal catalysts, such as Pt and Ir, exhibit outstanding ORR performance in fuel cell and metal-air battery, but its exorbitant cost, resource scarcity and poor stability severely impede the large-scale commercial applications [12, 16, 18–20]. Hence, developing efficient non-noble ORR catalysts is very crucial to replace the noble-metal catalysts and apply in Mg-air batteries.

Prussian blue analogues (PBA), assembled by transition metal ions and N-containing ligands, have aroused extensive attention in recent years due to tunable composition, structural stability, controllable morphology, easy preparation and low cost [21–23]. PBA have been regarded as the promising precursor and extensively applied in the fields of electrocatalysts [24], water splitting [25], fuel cells [26], Li-ion [27] and metal-air batteries [25, 28–30] because of the unique properties. Meanwhile, the PBA with the opening framework structure have been used as the precursor to synthesize transition metal composite

oxides [31, 32]. Transition metal composite oxides are one of the most promising candidate for non-noble metal ORR catalysts due to the wide potential window, good electrochemical redox activity, outstanding stability and low cost [19, 33, 34]. However, the poor electrical conductivity severely restricts the ORR activities [35]. The high conductivity carbonaceous materials are generally used as supports to improve their conductivity and enhance the ORR activity [33]. Furthermore, the mixed metal oxides can elevate the ORR activity compared with single metal oxides, which attributes to the presence of multi valence states, more active sites and synergistic effect between different metals [35–38]. It is a simple and effective strategy to synthesize mixed metal oxides using PBA as precursor. But there are few studies on the synthesis of mixed metal oxides as ORR catalysts using PBA precursor.

In this work, the $\text{CuO@Co}_3\text{O}_4$ composite oxide was successfully synthesized by calcining the CuCo-based PBA precursor in the air. The $\text{CuO@Co}_3\text{O}_4$ nanoparticles display better ORR activities in alkaline and neutral medium compared with the CuCo-based PBA. The experimental results suggest that the electrochemical performance of CCO-600 is competitive to the commercial Pt catalyst in alkaline electrolyte among these as-prepared catalysts in this study. The primary Mg-air battery was assembled with the CCO-600 as the cathode catalyst and showed excellent discharge performance. This work provides a facile and straightforward method to design transition metal composite oxides as efficient non-noble metal ORR catalyst, which is also worthy to explore the potential application of these catalysts in metal-air batteries.

2 Experimental Section

2.1 Synthesis of CuCo-based PBA nanocubes

Uniform CuCo-based PBA nanocubes (CuCo-PBA) were successfully fabricated via a facile one-step chemical precipitation method. In brief, 6.0 mmol $\text{Cu}(\text{NO}_3)_2 \cdot 3\text{H}_2\text{O}$ and 9.0 mmol $\text{K}_3\text{C}_6\text{H}_5\text{O}_7 \cdot \text{H}_2\text{O}$ were dissolved in 200 mL deionized (DI) water with stirring for 30 mins to form a transparent blue solution and denoted as solution A. Then, 4 mmol $\text{K}_3[\text{Co}(\text{CN})_6]$ was added in 200 mL DI water with stirring for 30 mins to become a homogeneous yellow solution B. The solution B was tardily dropped into the solution A with vigorous stirring and kept for 0.5 h. The above mixed solution remained aging for 24 h at room temperature. The resulting blue sediments were collected with centrifugation and washed by DI water and ethanol for several times, and then dried in a vacuum oven at 80 °C 12 h to obtain CuCo-PBA sample.

2.2 Preparation of $\text{CuO@Co}_3\text{O}_4$ nanoparticles

The CuCo-PBA samples were calcined at different temperatures to obtain a series of $\text{CuO@Co}_3\text{O}_4$ nanoparticles. The CuCo-PBA nanocubes were pyrolyzed in a muffle furnace with a heating rate of 5 °C·min⁻¹ to 400 °C, 600 °C and 800 °C for 2 h in the air to obtain $\text{CuO@Co}_3\text{O}_4$ nanoparticles. The corresponding samples were denoted as CCO-400, CCO-600 and CCO-800, respectively.

2.3 Materials characterization

X-ray diffraction (XRD, Rigaku D/max 2500PC, Cu K α radiation) was performed to characterize the crystalline phase and chemical composition of samples. X-ray photoelectron spectroscopy (XPS, ESCALAB 250Xi) spectra were conducted to explore the chemical elements and surface valence state of as-prepared catalyst. The XPS spectra of catalyst were corrected by the binding energy of C 1s at 284.8 eV. The morphology and structure of as-prepared catalysts were observed by field emission scanning electron microscope (SEM, JSM-7800F) and transmission electron microscopy (TEM, FEI Talos F200S G2).

2.4 Electrochemical measurements

The electrochemical performance of as-prepared catalysts was determined with an electrochemical workstation (RST, 5100F) equipped with a rotating disk electrode (RDE) device under identical test condition. A classic three-electrode configuration was conducted to the electrochemical measurements, making up of Pt electrode, Ag/AgCl (saturated KCl solution) electrode and catalyst ink supported glassy carbon (GC) electrode (5 mm in diameter), as counter electrode, reference electrode and working electrode, respectively.

For preparing the homogeneous ink of catalyst, the 5.0 mg as-prepared sample and 5.0 mg Ketjen black were dispersed in the blend solution of 950 μ L absolute ethyl alcohol and 50 μ L Nafion solution (5.0 wt%) under ultrasonic processing for 1.0 h. Then, 10 μ L of catalyst ink was pipetted and slowly dropped on the center of GC electrode and formed an even film with the catalyst loading of 250 μ g \cdot cm $^{-2}$ at room temperature. The electrochemical performance of as-obtained catalysts was evaluated in 0.1 M KOH and 3.5 wt% NaCl solution as electrolyte, severally. All measured potentials based on Ag/AgCl electrode have been converted to reversible hydrogen electrode (RHE) depending on the Nernst equation: $E_{\text{RHE}} = E_{\text{Ag/AgCl}} + 0.059 \text{ pH} + E_{\text{Ag/AgCl}}^0$ ($E_{\text{Ag/AgCl}}^0 = 0.197 \text{ V}$ at 25 $^{\circ}\text{C}$). Besides, the electrochemical impedance spectroscopy (EIS) was conducted with the frequency from 0.01 to 1000 kHz at an amplitude of 5 mV. All the electrochemical test results were not corrected by IR compensation in this work.

2.5 Mg-air battery

In order to evaluate the application potential of as-synthesized catalysts in metal-air battery, a primary Mg-air battery was made up of self-assembly air cathode, electrolyte and metal anode. The air cathode was constituted of gas diffusion layer, conductive collector layer and catalyst layer. The hydrophobic carbon paper (YLS-30T) was used as gas diffusion and conductive collector layer. As for catalyst layer, the catalyst, Ketjen black, NaHCO $_3$ and PVDF were dispersed in N-N dimethylamide solution with a mass ratio of 6:1:1:2 to form a homogenous slurry. The slurry was uniformly coated on carbon paper and dried at 80 $^{\circ}\text{C}$ 12 h to obtain the air cathode. 3.5 wt% NaCl solution was served as the electrolyte and AZ31 Mg alloy as anode.

The test mold of Mg-air battery is 6.0 cm high, 7.0 cm wide, the distance between the cathode and anode is 1.4 cm, the liquid capacity is 12 mL, and the effective exposure area is 1.0 cm 2 . All Mg-air battery tests

were conducted on RST 5100F electrochemical workstation and Neware battery test systems at room temperature and without additional oxygen.

3 Results And Discussion

3.1 Structural and morphological characterization

The CuCo-PBA and CuO@Co₃O₄ were synthesized with a simple chemical precipitation method and subsequent calcination. The crystalline characterizations of as-obtained samples were conducted by XRD analysis and the corresponding XRD patterns are displayed in Fig. 1. As can be seen from Fig. 1, the pattern of CuCo-PBA exhibits distinct diffraction peaks at 15.3°, 17.7°, 25.1°, 35.7°, 40.1°, 44.2°, 51.4°, 54.8° and 58.1°, which can be well indexed to the (111), (200), (220), (400), (420), (422), (440), (600) and (620) lattice planes of Cu₃[Co(CN)₆]₂·9H₂O (JCPDF No.51-1895) [36], respectively. Meanwhile, the similar XRD patterns of CuO@Co₃O₄ samples calcined at different temperatures are recorded. Some diffraction peaks at 19.0°, 31.3°, 36.8°, 44.8° and 53.4° are matched with the (111), (220), (311), (400) and (511) planes of Co₃O₄ (JCPDF No.43-1003). The rest peaks at 35.5°, 38.9°, 48.7°, 53.4°, 59.4° and 68.0° are corresponded to the (-111), (111), (-202), (020), (-113) and (220) planes of CuO (JCPDS No.80-1916) [36, 39, 40]. This result indicates that the samples after calcination are the composite of CuO and Co₃O₄. The CuCo-PBA nanocube precursors are converted into the corresponding metal oxides after calcination in air.

The chemical constitution and elemental electronic state of CCO-600 were further employed by XPS measurement. The XPS spectra are displayed in Fig. 2. The full survey scan spectrum of CCO-600 is exhibited in Fig. 2(a) and confirmed the existence of Cu, Co, O and C elements without other elements. All the peaks of elements take C 1s peak (284.6 eV) as the reference. Fig. 2(b) represents the Cu 2p spectrum and shows two feature peaks at 933.4 and 953.4 eV, ascribing to the Cu 2p_{3/2} and Cu 2p_{1/2}. Besides, there are two obvious satellite peaks locating at 935 and 955 eV corresponding to the Cu²⁺, due to the existence of pure CuO [20, 41]. As revealed in Fig. 2(c), the distinct peaks at 782 and 796 eV are matched to the binding energies of Co 2p_{3/2} and Co 2p_{1/2}, demonstrating Co³⁺ and Co²⁺ electronic states for Co₃O₄ [27, 35]. Fig. 2(d) displays the O 1s spectrum. The characteristic peaks at 529.7 eV, 531.2 eV and 532.3 eV are defined as O_α, O_β and O_γ, corresponding to metal-oxygen bond and the surface hydroxyl species or the adsorbed oxygen [42]. The above results certify the existence of Cu²⁺, Co²⁺ and Co³⁺ ions on the surface of sample, suggesting the CCO-600 only contains CuO and Co₃O₄.

To observe the morphology and structure of as-obtained samples, the SEM and TEM were further conducted. Fig. 3(a-c) display the CuCo-PBA nanocubes with an average dimension around 1 μm at different magnifications. Fig. 3(d-f) reveal the morphology of CCO-400, CCO-600 and CCO-800, respectively. It is obvious that the smaller CuO@Co₃O₄ nanoparticles were obtained from the CuCo-PBA nanocube precursors calcining at different temperatures. The average size of CCO-400, CCO-600 and CCO-800 arrive at around 200, 100 and 500 nm, severally. Transformation of morphology from nanocube to nanoparticle caused by calcination could be explained by the evaporation of lattice water. It is known

to all that the smaller the average size of the catalyst, the more active sites it can provide. The CCO-600 has the smallest average size among those catalysts, which can offer larger specific surface area and increase the contact interface between electrode and electrolyte, boosting the ORR electronic and mass transfer process [30]. TEM image in Fig. 3(g) further illustrates that the average size of as-obtained CCO-600 nanoparticles are about 100 nm, which consist with the SEM results. The high-resolution TEM (HRTEM) and selected area electron diffraction (SAED) are shown in Fig. 3(h). The lattice fringes of 0.285, 0.243, 0.202 and 0.252 nm are matched to (220), (311), (400) crystal faces of Co_3O_4 and (-111) crystal plane of CuO [20, 36, 43], separately. The inset figure in Fig. 3(h) reveals the SAED pattern of the CCO-600, indicating a polycrystalline structure of catalyst. Furthermore, the TEM image and elemental mapping analysis are exhibited in Fig. 3(i) and confirmed the existence of Cu, Co and O elements and uniform distribution. The phenomenon is consistent with the XPS survey spectrum consequence.

3.2 Electrochemical characterization for ORR

To evaluate the ORR performance of as-obtained catalysts, the cyclic voltammetry (CV) measurements were preliminarily conducted in 0.1 M KOH electrolyte saturated by O_2 and N_2 at a scan rate of $20 \text{ mV}\cdot\text{s}^{-1}$ [30]. The corresponding CV curves of catalysts are illustrated in Fig. 4 and Fig. 5. As can be seen from the Fig. 5, all CV curves display significant oxygen reduction peaks in the O_2 -saturated electrolyte, while no noticeable reduction peaks are found in the N_2 -saturated electrolyte solution. The results confirm that these catalysts possess oxygen reduction activity in O_2 -saturated 0.1 M KOH solution [27]. Fig. 4 summarizes the CV curves of all catalysts under O_2 saturation condition, and it is found that the oxygen reduction peaks of CCO-400, CCO-600 and CCO-800 are more positive than CuCo-PBA. In particular, the CV curve of CCO-600 demonstrates the most positive reduction peak potential (about 0.66 V), indicating the CCO-600 may possess best ORR activity among these catalysts [25].

The linear sweep voltammetry (LSV) tests were performed to further explore ORR activities of catalysts by RDE in O_2 -saturated 0.1 M KOH solution [27, 30]. Fig. 6(a-d) reveals the LSV curves of CuCo-PBA, CCO-400, CCO-600 and CCO-800 at various rotating rates (400 to 2000 rpm) with a scan rate of $5 \text{ mV}\cdot\text{s}^{-1}$ (0.2 to 1.2 V vs RHE). With the increase of rotating rate, the diffusion limiting current density of catalysts constantly enhances because of shortening of the diffusion distance and promoting mass transport rate at GC electrode surface, signifying the ORR process of catalysts follows a first-order kinetic process [26, 27]. The onset potential (E_{onset}) is denoted as the potential at the current density of $0.10 \text{ mA}\cdot\text{cm}^{-2}$ in this work. Fig. 6(e) displays the LSV curves of these catalysts and commercial Pt at 1600 rpm in O_2 -saturated electrolyte. The onset and half-wave potentials of as-prepared CCO-600 (0.889 V, 0.665 V) are visibly higher than those of the CuCo-PBA (0.759 V, 0.620 V), CCO-400 (0.826 V, 0.654 V) and CCO-800 (0.771 V, 0.618 V), evidencing the ORR activity of CCO-600 outperform other catalysts. Besides, the onset potential of CCO-600 is 0.889 V, which is merely 57 mV more negative than commercial Pt. Moreover, the CCO-600 also reveals an outstanding limit current density of $6.746 \text{ mA}\cdot\text{cm}^{-2}$ at 0.164 V compared with CuCo-PBA ($4.311 \text{ mA}\cdot\text{cm}^{-2}$), CCO-400 ($4.627 \text{ mA}\cdot\text{cm}^{-2}$) and CCO-800 ($5.331 \text{ mA}\cdot\text{cm}^{-2}$). It deserves to note that the limit current density of CCO-600 ($6.746 \text{ mA}\cdot\text{cm}^{-2}$) at 0.164 V exceeds that of the commercial Pt (5.824

$\text{mA}\cdot\text{cm}^{-2}$), which can be attributed to the synergistic effect between CuO with Co_3O_4 and affluent active sites [32, 35–37]. The above results illustrates the CCO-600 is the most excellent ORR catalyst among those electrocatalysts and is accord with the CV results.

To further investigate the ORR reaction mechanism of as-obtained catalysts, the corresponding Koutecky-Levich (K-L) curves at various potentials were drew from the LSV plots at different rotate speeds [17, 24, 26]. Fig. 6(f) and (g) show the K-L curves of CuCo-PBA and CCO-600, severally. The K-L curves of CCO-600 exhibit good linearity and almost identical slopes from 0.2 to 0.5 V vs RHE compared with CuCo-PBA, suggesting a steady kinetic reaction process and first-order reaction dynamic mechanism [37, 44]. Furthermore, the transfer electron number (n) is a crucial index to estimate the ORR activity of as-obtained catalysts and can be calculated by the K-L equations as follow:

$$\frac{1}{j} = \frac{1}{j_k} + \frac{1}{B\omega^{1/2}} \quad (1)$$

$$B = 0.2nFD^{2/3}u^{-1/6} C \quad (2)$$

where j and j_k refer to the observed current density and the kinetic current density severally. ω represents the rotation rate, n expresses the transfer electron number. F and D mean the Faraday constant ($96,485 \text{ C mol}^{-1}$) and O_2 diffusivity in 0.1 M KOH ($1.9 \times 10^{-5} \text{ cm}^2 \text{ s}^{-1}$) respectively, u is the kinematic viscosity of 0.1 M KOH ($0.01 \text{ cm}^2\text{s}^{-1}$), C is the bulk concentration of O_2 ($1.2 \times 10^{-6} \text{ mol cm}^{-3}$) [12, 27, 30, 44]. The Fig. 6(h) displays that the n value of CuCo-PBA, CCO-400, CCO-600, CCO-800 and Pt are around 2.91, 3.53, 3.89, 4.24 and 4.02, severally. The ORR process of CCO-400, CCO-600, CCO-800 is dominated a quasi-four-electron reaction pathway and the catalytic mechanism is equivalent to the commercial Pt catalyst [27]. In addition to the catalytic activity of ORR, the cyclic stability of the catalyst is also an important indicator [32, 45]. As revealed in Fig. 6(i), the CCO-600 demonstrates outstanding durability and stability in 0.1 M KOH solution. Its half-wave potential merely has a negative shift of 13 mV after 5000 cycles. The above results indicate that CCO-600 catalyst has tremendous application potential as a non-noble metal ORR catalyst.

The electrochemical impedance spectroscopy (EIS) measurements were also carried out at 0.60 V to demonstrate the different ORR kinetics of as-prepared catalysts. The Nyquist impedance spectra of catalysts were revealed in Fig. 7, which are all comprised of the semicircle and sloping line at high and low frequency region, severally. The diameter of the semicircle can represent the value of the interface charge transfer resistance (R_{ct}) and the slope of the line can represent the solution resistance (R_s) [32, 45]. The R_{ct} and R_s of CCO-600 catalyst are smallest among those catalysts as seen from in Fig. 7, manifesting the highest electron transfer capacity and the fastest electrical kinetics for CCO-600 catalyst during ORR [36, 46]. The main reasons are attributed to the synergistic effect between CuO with Co_3O_4 and the specific surface area of CCO-600 catalyst. The synergistic effect of catalyst can facilitate the

electron transfer and the large specific surface area can provide sufficient contact between the catalyst and the electrolyte, leading to the smaller impedance.

In this work, the ORR activity under neutral condition (3.5 wt% NaCl electrolyte) was also measured to explore the potential application of CCO-600 catalyst as cathode catalyst for Mg-air batteries. Fig. 8 exhibits the CV curves in O₂-saturated NaCl solution. The reduction peaks of CuCo-PBA, CCO-400, CCO-600 and CCO-800 locates at 0.352 V, 0.365 V, 0.370 V and 0.363 V severally, and the CCO-600 possesses the most positive potential which demonstrates the best ORR activity.

Figure 9(a-d) represent the LSV curves of different catalysts in 3.5 wt% NaCl solution at various rotate speeds with a scan rate of 5 mV s⁻¹ (0.0 to 1.0 V vs RHE). The diffusion limiting current density is constantly enhanced with the increasing of rotating speeds which also demonstrates the ORR pathway of catalyst is controlled by kinetic [27, 44]. Figure 9(e) displays the LSV curves of as-obtained catalysts in NaCl solution at 1600 rpm. The onset and half-wave potentials of CCO-600 (0.560 V, 0.376 V) exceed CuCo-PBA (0.508 V, 0.347 V), CCO-400 (0.541 V, 0.364 V) and CCO-800 (0.534 V, 0.355 V), certifying the ORR performance of CCO-600 is better than other catalysts. Moreover, the stability and durability of CCO-600 were performed in Figure 9(f) and half-wave potential only has a minus shift of 20 mV after 5000 cycles. The above results illustrate the CCO-600 still has the best ORR catalytic activity in 3.5 wt% NaCl electrolyte and may be an outstanding cathode catalyst for Mg-air batteries.

3.3 Application in Mg-air battery

The CCO-600 catalyst may have great potential as a cathode catalyst for Mg-air battery due to excellent ORR performance. A primary Mg-air battery was assembled with 1 mm thick AZ31 Mg alloy plate as anode, 3.5 wt% NaCl as electrolyte and self-assembled cathode. The CuCo-PBA catalyst was also applied to air cathode under the same condition for comparison. Fig. 10(a) reveals the open circuit voltage (OCV) of batteries and the CCO-600-based battery keeps around 1.76 V after running for 30 mins and CuCo-PBA-based battery is maintained at about 1.66 V. Fig. 10(b) presents the discharge curves of CuCo-PBA and CCO-600 assembled batteries at the current densities of 1.0 mA·cm⁻², 5.0 mA·cm⁻² and 10.0 mA·cm⁻². The working voltage of batteries continuously decreases following the increase of current density which ascribes to ohmic polarization [14, 46]. The average discharge voltages of CuCo-PBA arrive around 1.19 V, 1.07V and 0.96 V and the CCO-600 maintains around 1.25 V, 1.13 V and 1.02 V at the current densities of 1.0 mA·cm⁻², 5.0 mA·cm⁻² and 10.0 mA·cm⁻², respectively. The power density, specific capacity density and energy density of primary batteries assembled with two catalysts were calculated by the effective anode quality and summarized in Table 1. As can be seen, the discharge performance of the batteries assembled by CCO-600 is better than that of the batteries assembled by CuCo-PBA. It is also proved that the CCO-600 has a better ORR performance than the CuCo-PBA, which is consistent with the previous ORR performance test results.

Table 1

The discharge performance of Mg-air batteries with different cathode catalysts in this work.

Current density (mA/cm ²)	Power density (mW/cm ²)	Specific capacity density (mAh/g)	Energy density (mWh/g)
CuCo-PBA CCO-600 CuCo-PBA CCO-600 CuCo-PBA CCO-600			
1.0	1.19 1.25	1521.98 1516.75	1811.15 1895.95
5.0	5.35 5.65	1249.36 1283.62	1336.82 1450.49
10.0	9.60 10.20	1313.40 1371.08	1260.90 1398.49

In addition, the stability and durability of cathode catalyst are very crucial indexes to influence the service life of Mg-air batteries [13]. As the Fig. 10(b) depicted, the Mg-air batteries assembled with CCO-600 have extremely stable discharge plateau and higher operating voltage at different current densities compared with the CuCo-PBA, which reveals greatly outstanding discharge behavior, demonstrating its excellent catalytic stability and durability. The above results further suggest that the better ORR catalytic activity of CCO-600 can improve the Mg-air battery performance compared with CuCo-PBA. Hence, the CCO-600 has been proofed to be an effective non-noble metal catalyst in the practical application of Mg-air battery and provides a very simple method for the synthesis of the non-noble ORR electrocatalysts.

4 Conclusion

A facile and effective strategy has been applied to synthesize CuO@Co₃O₄ nanoparticles by calcining CuCo-PBA nanocubes and used as highly active cathode catalyst for Mg-air battery. The electrochemical measurements manifest the CCO-600 catalyst possesses the most excellent catalytic activities toward ORR compared with others catalysts in this work whether in alkaline or neutral electrolyte. The onset potential of CCO-600 is 0.889 V which is merely 57 mV more negative than commercial Pt and the diffusion limiting current density of CCO-600 (6.746 mA·cm⁻²) even surpasses the commercial Pt (5.824 mA·cm⁻²) in alkaline medium. The half-wave potential has only 13 and 20 mV negative deviation after 5000 cycles in alkaline and neutral electrolytes, respectively. The CCO-600 catalyst reveals superior ORR activity and outstanding stability in both alkaline and neutral electrolytes which attributes to the synergistic effect between CuO with Co₃O₄ and large specific surface area exposing more active sites. The Mg-air battery assembled by the CCO-600 catalyst as cathode catalyst exhibits excellent discharge performance such as high open circuit voltage, operating voltage and good energy density, demonstrating the potential for practical application. This work provides a promise strategy to synthesis non-noble metal ORR catalyst for the development of metal-air batteries.

Declarations

Acknowledgment

The authors sincerely gratitude the economic support supplied by the Fundamental Research Funds for the Central Universities (No.2021CDJKYJH001 and 2019CDYGYB018).

References

1. Zhang S, Chen M, Zhao X, *et al.* Advanced Noncarbon Materials as Catalyst Supports and Non-noble Electrocatalysts for Fuel Cells and Metal-Air Batteries. *Electrochem Energy R* 2021, **2**: 336–381.
2. Zhao C X, Liu J N, Wang J, *et al.* Recent advances of noble-metal-free bifunctional oxygen reduction and evolution electrocatalysts. *Chem Soc Rev* 2021, **13**: 7745–7778.
3. Lu YT, Neale AR, Hu CC, *et al.* Divalent Nonaqueous Metal-Air Batteries. *Front Energy Res* 2021, **8**: 602918.
4. Liu Q, Pan Z, Wang E, *et al.* Aqueous metal-air batteries: Fundamentals and applications. *Energy Storage Mater* 2020, **27**: 478–505.
5. Ling W, Wang H, Chen Z, *et al.* Intrinsic Structure Modification of Electrode Materials for Aqueous Metal-Ion and Metal-Air Batteries. *Adv Funct Mater* 2020, **31**: 2006855.
6. Sun Y, Liu X, Jiang Y, *et al.* Recent advances and challenges in divalent and multivalent metal electrodes for metal–air batteries. *J Mater Chem A* 2019, **7**: 18183–18208.
7. Zhu B, Liang Z, Xia D, *et al.* Metal-organic frameworks and their derivatives for metal-air batteries. *Energy Storage Mater* 2019, **23**: 757–771.
8. Li CS, Sun Y, Gebert F, *et al.* Current Progress on Rechargeable Magnesium-Air Battery. *Adv Energy Mater* 2017, **7**: 1700869.
9. Zhang T, Tao Z, Chen J, Magnesium-air batteries: from principle to application. *Mater Horiz.* 2014, **1**: 196–206.
10. Mo ZY, Yang WY, Gao S, *et al.* Efficient oxygen reduction reaction by a highly porous, nitrogen-doped carbon sphere electrocatalyst through space confinement effect in nanopores. *J Adv Ceram* 2021, **10**: 714–728.
11. Li L, Chen H, He E, *et al.* High-energy-density Magnesium-air Battery Based on Dual-layer Gel Electrolyte. *Angew Chem Int Ed Engl* 2021, **60**: 15317–15322.
12. Li Y, Zhang X, Li HB, *et al.* Mixed-phase mullite electrocatalyst for pH-neutral oxygen reduction in magnesium-air batteries. *Nano Energy* 2016, **27**: 8–16.
13. Zhao X, Wang L, Chen X, *et al.* Ultrafine $\text{SmMn}_2\text{O}_{5.6}$ electrocatalysts with modest oxygen deficiency for highly-efficient pH-neutral magnesium-air batteries. *J Power Sources* 2020, **449**: 227482.
14. Ma J, Qin C, Li Y, *et al.* Properties of reduced graphene oxide for Mg-air battery. *J Power Sources* 2019, **430**: 244–251.
15. Wen X, Zhang Q, Guan J, Applications of metal-organic framework-derived materials in fuel cells and metal-air batteries. *Coordin Chem Rev* 2020, **409**: 213214.
16. Wang J, Kong H, Zhang J, *et al.* Carbon-based electrocatalysts for sustainable energy applications. *Prog Mater Sci* 2021, **116**: 100717.

17. Xu N, Nie Q, Luo L, *et al.* Controllable Hortensia-like MnO₂ Synergized with Carbon Nanotubes as an Efficient Electrocatalyst for Long-Term Metal-Air Batteries. *ACS Appl Mater Inter* 2019, **11**: 578–587.
18. Xie C, Niu Z, Kim D, *et al.* Surface and Interface Control in Nanoparticle Catalysis. *Chem Rev.* 2020, **120**: 1184–1249.
19. Wang HF, Chen L, Pang H, *et al.* MOF-derived electrocatalysts for oxygen reduction, oxygen evolution and hydrogen evolution reactions. *Chem Soc Rev* 2020, **49**: 1414–1448.
20. Harilal M, Vidyadharan B, Misnon II, *et al.* One-Dimensional Assembly of Conductive and Capacitive Metal Oxide Electrodes for High-Performance Asymmetric Supercapacitors. *ACS Appl Mater Inter* 2017, **9**: 10730–10742.
21. Chen J, Wei L, Mahmood A, *et al.* Prussian blue, its analogues and their derived materials for electrochemical energy storage and conversion. *Energy Storage Mater* 2020, **25**: 585–612.
22. He Y, Wang Z, Wang H, *et al.* Metal-organic framework-derived nanomaterials in environment related fields: Fundamentals, properties and applications. *Coordin Chem Rev* 2021, **429**: 213618.
23. Ma F, Li Q, Wang T, *et al.* Energy storage materials derived from Prussian blue analogues. *Sci Bull* 2017, **62**: 358–368.
24. Zhao D, Dai J, Zhou N, *et al.* Prussian blue analogues-derived carbon composite with cobalt nanoparticles as an efficient bifunctional electrocatalyst for oxygen reduction and hydrogen evolution. *Carbon* 2019, **142**: 196–205.
25. Niu HJ, Chen YP, Sun RM, *et al.* Prussian blue analogue-derived CoFe nanocrystals wrapped in nitrogen-doped carbon nanocubes for overall water splitting and Zn-air battery. *J Power Sources* 2020, **480**: 229107.
26. Zhang X, Lin Z, Liang B, *et al.* Highly efficient improvement of power generation and waste removal in microbial fuel cell by associating activated carbon with a novel porous iron-nitrogen-doped carbon nanosphere. *J Power Sources* 2021, **498**: 229883.
27. Meng D, Zhang C, Liang Y, *et al.* Electrospun cobalt Prussian blue analogue-derived nanofibers for oxygen reduction reaction and lithium-ion batteries. *J Colloid Interf Sci* 2021, **599**: 280–290.
28. Zhang J, Lyu ZY, Zhang F, *et al.* Facile synthesis of hierarchical porous Co₃O₄ nanoboxes as efficient cathode catalysts for Li-O₂ batteries. *J Mater Chem A* 2016, **4**: 6350–6356.
29. Najam T, Wang M, Javed MS, *et al.* Nano-engineering of prussian blue analogues to core-shell architectures: Enhanced catalytic activity for zinc-air battery. *J Colloid Interf Sci* 2020, **578**: 89–95.
30. Cui L, Chen M, Huo G, *et al.* FeCo nanoparticles wrapped in N-doped carbon derived from Prussian blue analogue and dicyandiamide as efficient oxygen reduction electrocatalysts for Al-air batteries. *Chem Eng J* 2020, **395**: 125158.
31. Deng C, Wang DW, Functional Electrocatalysts Derived from Prussian Blue and its Analogues for Metal-Air Batteries: Progress and Prospects. *Batteries Supercaps* 2019, **2**: 290–310.
32. Zhang Y, Sun Y, Cai Z, *et al.* Stable CuO with variable valence states cooperated with active Co⁽²⁺⁾ as catalyst/co-catalyst for oxygen reduction/methanol oxidation reactions. *J Colloid Interf Sci* 2021,

593: 345–358.

33. Zhang YL, Goh K, Zhao L, *et al.* Advanced non-noble materials in bifunctional catalysts for ORR and OER toward aqueous metal-air batteries. *Nanoscale* 2020, **12**: 21534–21559.
34. Xue Y, Sun S, Wang Q, *et al.* Transition metal oxide-based oxygen reduction reaction electrocatalysts for energy conversion systems with aqueous electrolytes. *J Mater Chem A* 2018, **6**: 10595–10626.
35. Hazarika KK, Yamada Y, Matus EV, *et al.* Enhancing the electrocatalytic activity via hybridization of Cu(I/II) oxides with Co₃O₄ towards oxygen electrode reactions. *J Power Sources* 2021, **490**: 229511.
36. Duan LF, Gao FH, Wang LM, *et al.* Hydrothermal synthesis and characterization of MnCo₂O₄ in the low-temperature hydrothermal process: Their magnetism and electrochemical properties. *J Adv Ceram* 2013, **2**: 266–273.
37. Xiao J, Chen C, Xi J, *et al.* Core-shell Co@Co₃O₄ nanoparticle-embedded bamboo-like nitrogen-doped carbon nanotubes (BNCNTs) as a highly active electrocatalyst for the oxygen reduction reaction. *Nanoscale* 2015, **7**: 7056–7064.
38. Zhou Y, Zhang Y, Li Z, *et al.* Oxygen reduction reaction electrocatalysis inducing Fenton-like processes with enhanced electrocatalytic performance based on mesoporous ZnO/CuO cathodes: Treatment of organic wastewater and catalytic principle. *Chemosphere* 2020, **259**: 127463.
39. Wu M, Chen H, Lv LP, *et al.* Graphene quantum dots modification of yolk-shell Co₃O₄@CuO microspheres for boosted lithium storage performance. *Chem Eng J* 2019, **373**: 985–994.
40. Pradhan AC, Uyar T, Morphological Control of Mesoporosity and Nanoparticles within Co₃O₄-CuO Electrospun Nanofibers: Quantum Confinement and Visible Light Photocatalysis Performance. *ACS Appl Mater Inter* 2017, **9**: 35757–35774.
41. Cheng S, Delacruz S, Chen C, *et al.* Hierarchical Co₃O₄/CuO nanorod array supported on carbon cloth for highly sensitive non-enzymatic glucose biosensing. *Sensors Actuat B: Chem* 2019, **298**: 126860.
42. Liu K, Huang X, Wang H, *et al.* Co₃O₄-CeO₂/C as a Highly Active Electrocatalyst for Oxygen Reduction Reaction in Al-Air Batteries. *ACS Appl Mater Inter* 2016, **8**: 34422–34430.
43. Nguyen CD, Nguyen VH, Tuyen PNK, *et al.* Snowflake Co₃O₄-CuO heteroanode arrays supported on three-dimensional framework for enhanced oxygen evolution. *Electroanal Chem* 2020, **871**: 114235.
44. Wang X, Zou L, Fu H, *et al.* Noble Metal-Free Oxygen Reduction Reaction Catalysts Derived from Prussian Blue Nanocrystals Dispersed in Polyaniline. *ACS Appl Mater Inter* 2016, **8**: 8436–8444.
45. Wang YJ, Fan H, Ignaszak A, *et al.* Compositing doped-carbon with metals, non-metals, metal oxides, metal nitrides and other materials to form bifunctional electrocatalysts to enhance metal-air battery oxygen reduction and evolution reactions. *Chem Eng J* 2018, **348**: 416–437.
46. Mayilvel Dinesh M, Saminathan K, Selvam M, *et al.* Water soluble graphene as electrolyte additive in magnesium-air battery system. *J Power Sources* 2015, **276**: 32–38.

Figures

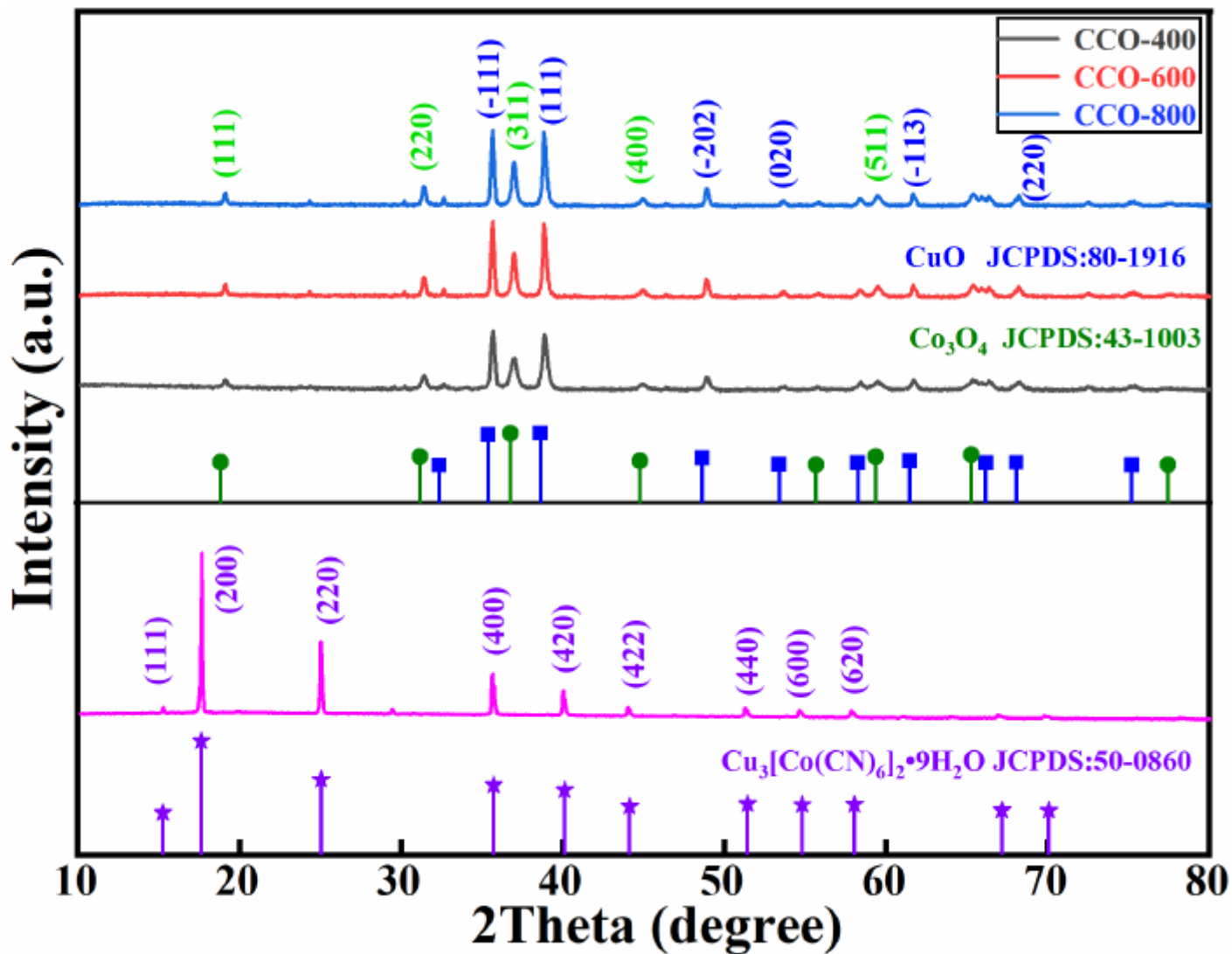


Figure 1

XRD patterns of the as-obtained catalysts.

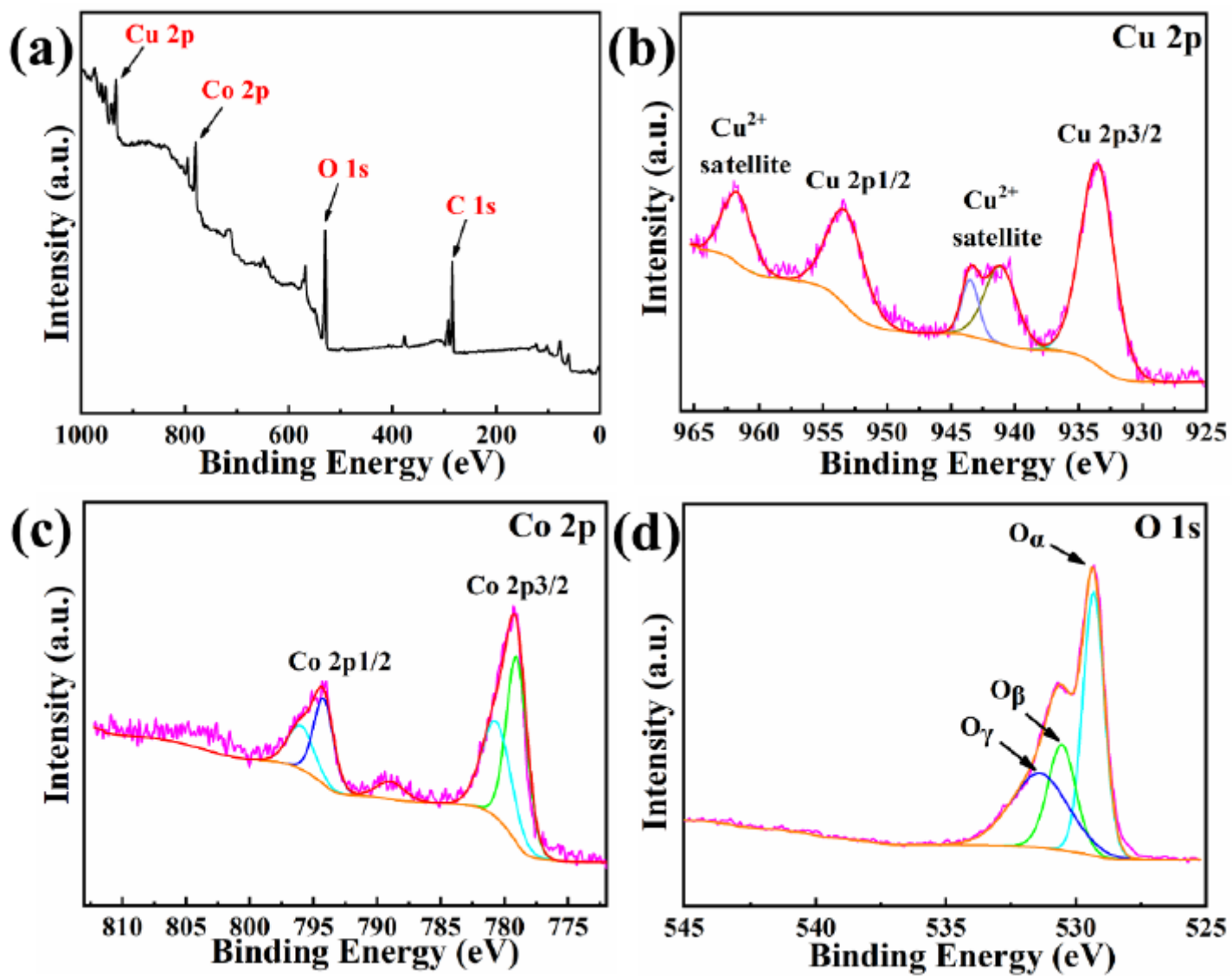


Figure 2

XPS spectra of the CCO-600 catalyst. (a) full XPS survey spectrum. (b) Cu 2p. (c) Co 2p. (d) O 1s.

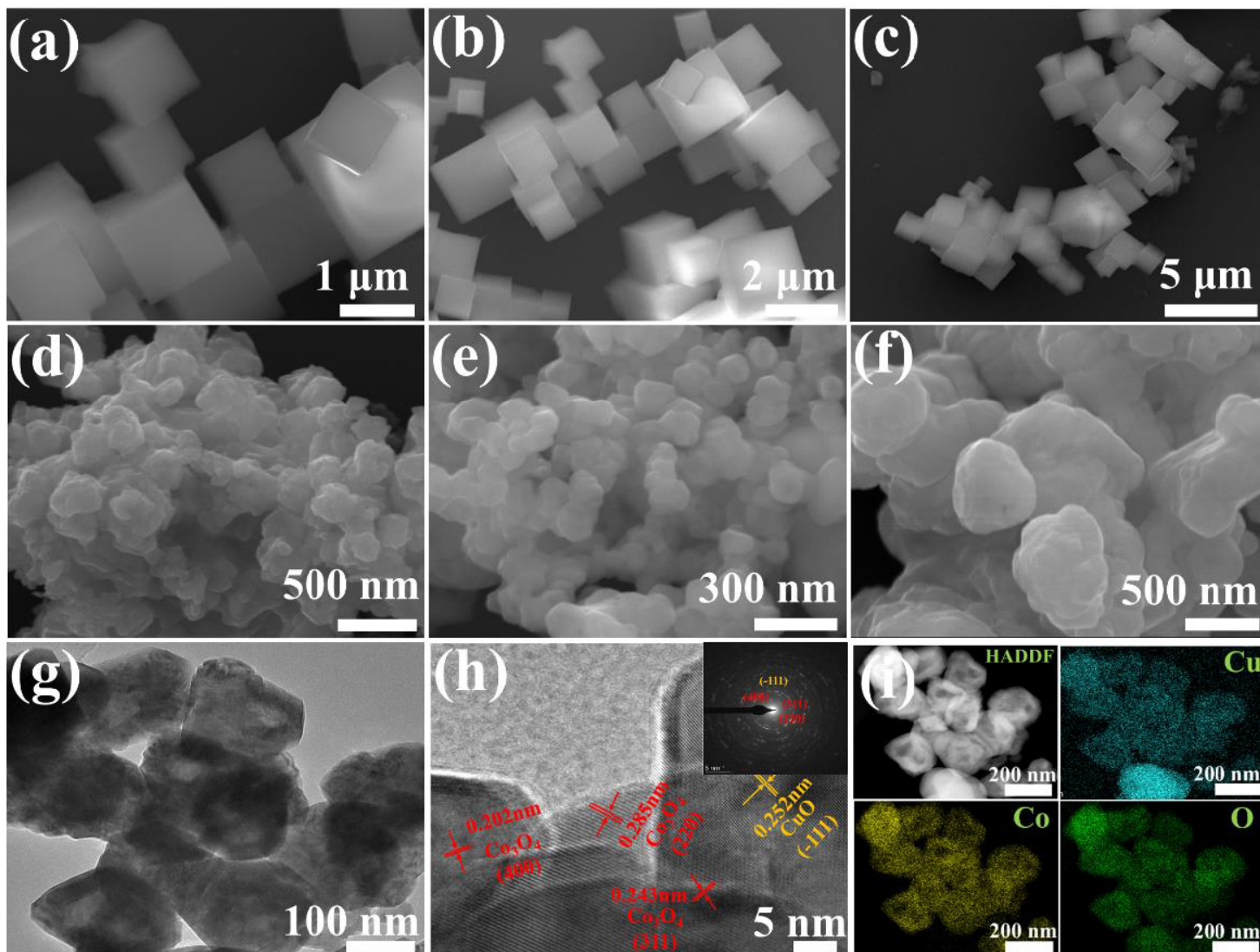


Figure 3

(a-c) SEM images of the CuCo-PBA. (d) SEM image of the CCO-400. (e) SEM image of the CCO-600. (f) SEM image of the CCO-800. (g) the TEM image of the CCO-600. (g-h) the HRTEM image of the CCO-600 (inset: the corresponding SAED pattern). (i) the EDS mapping of the CCO-600.

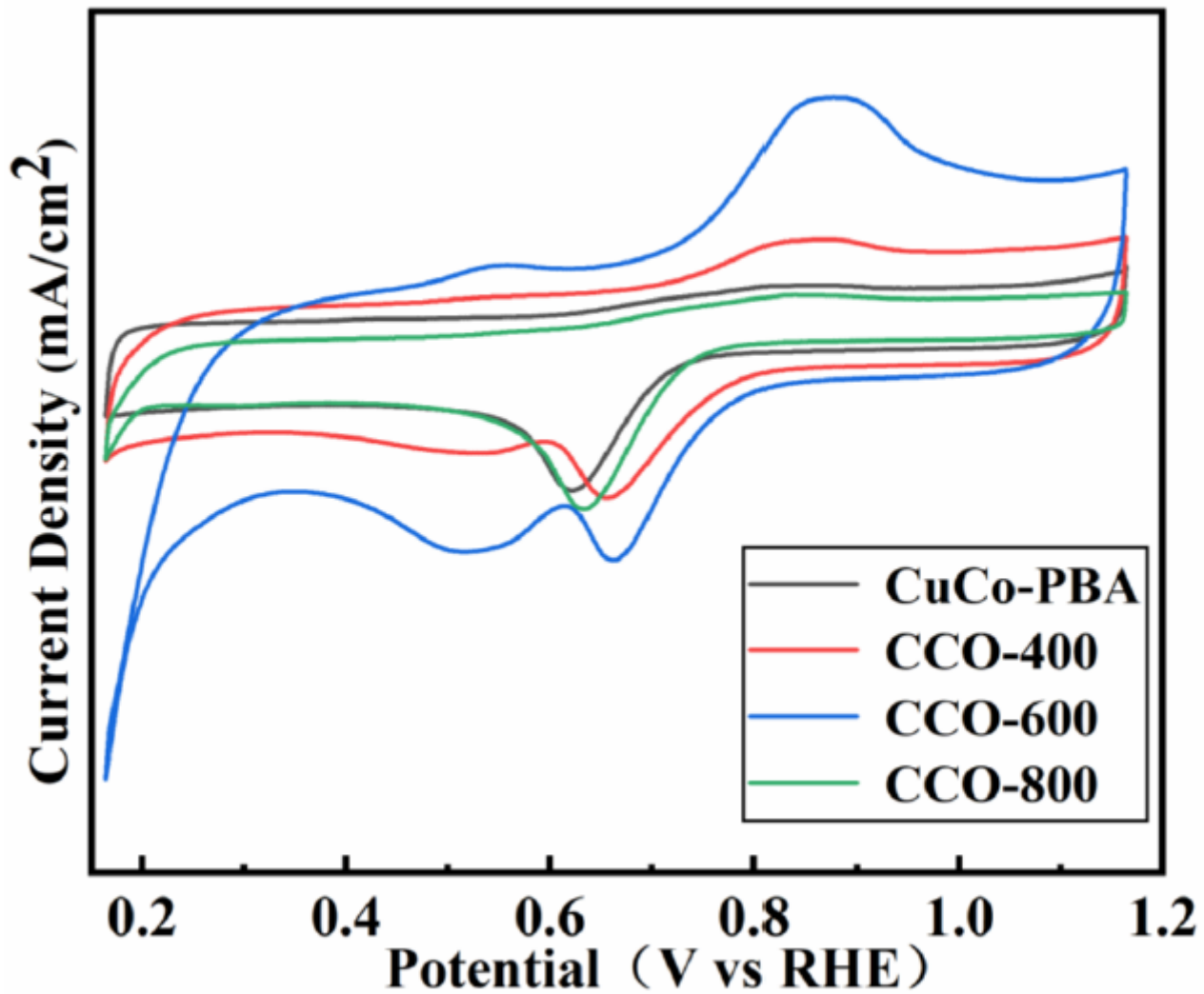


Figure 4

CV curves of various catalysts in O₂ saturated 0.1 M KOH solution.

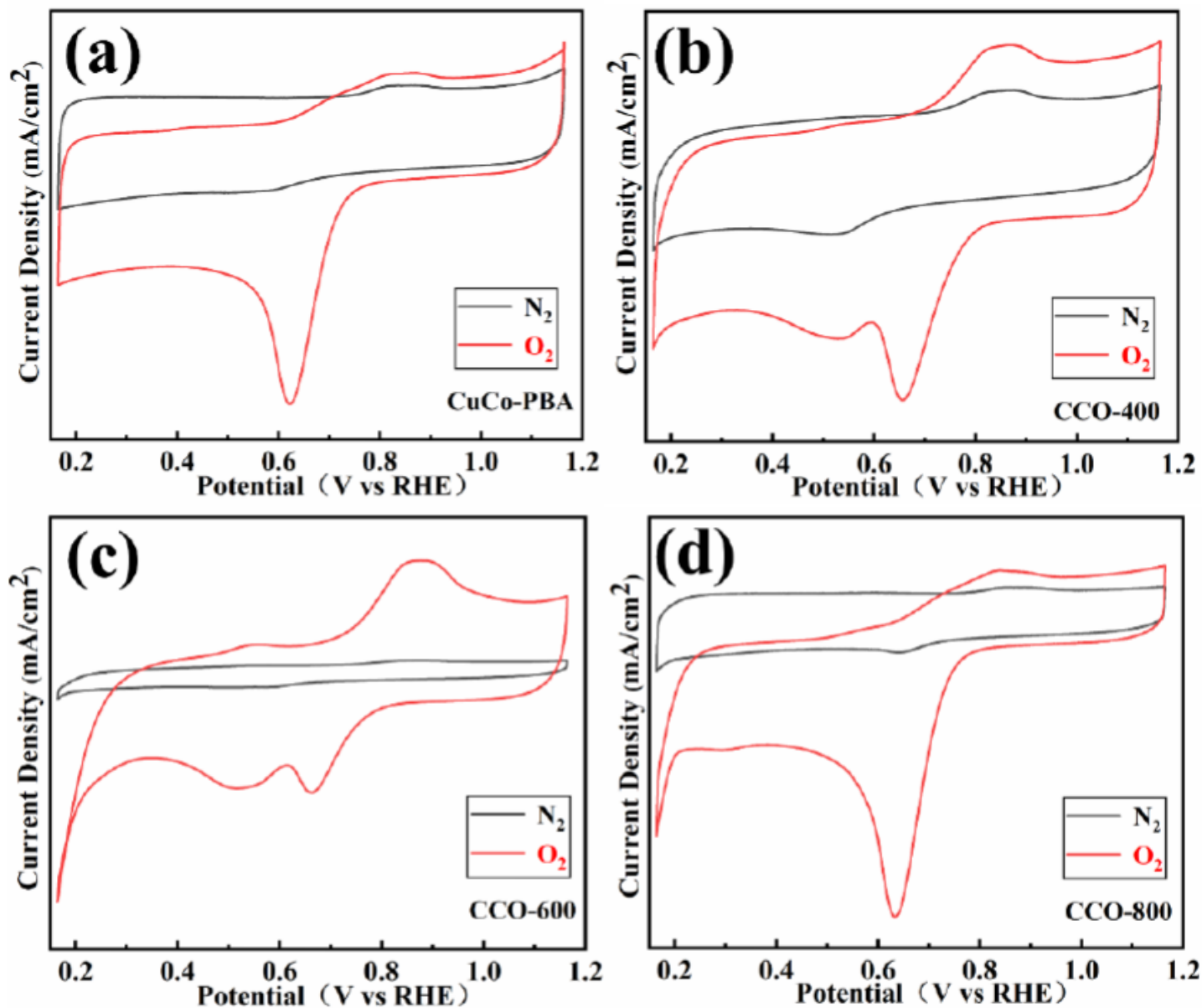


Figure 5

(a) CV curves of the CuCo-PBA. (b) CV curves of the CCO-400. (c) CV curves of the CCO-600. (d) CV curves of the CCO-800.

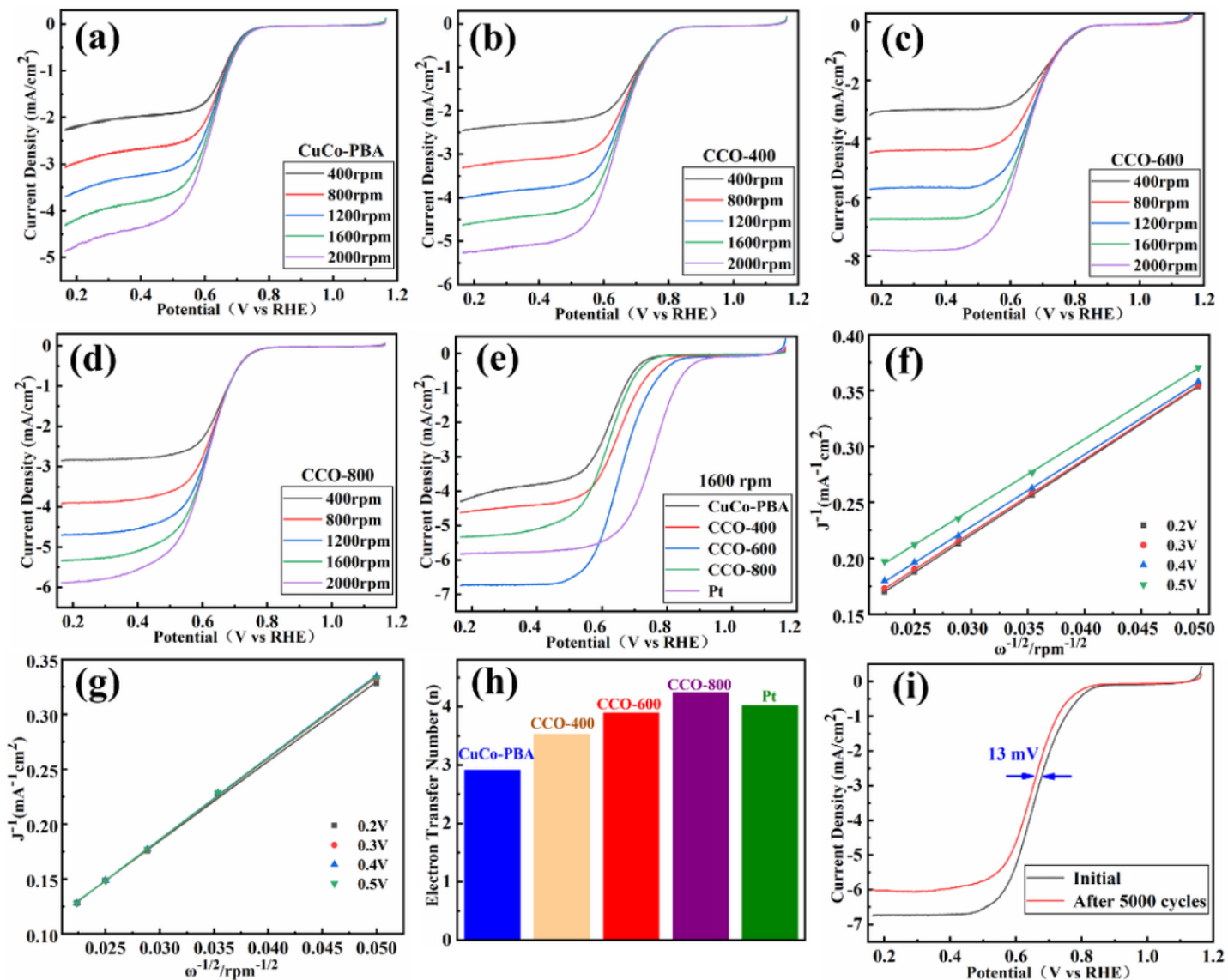


Figure 6

(a) LSV curves of the CuCo-PBA. (b) LSV curves of the CCO-400. (c) LSV curves of the CCO-600. (d) LSV curves of the CCO-800 at different rotate speeds. (e) LSV curves of various catalysts with a 1600 rpm rotate speed. (f) the K-L plots of the CuCo-PBA at different potentials. (g) the K-L plots of the CCO-600 at different potentials. (h) the transfer electron number of as-prepared catalysts and the commercial Pt catalyst. (i) LSV curves of the CCO-600 before and after 5000 cycles.

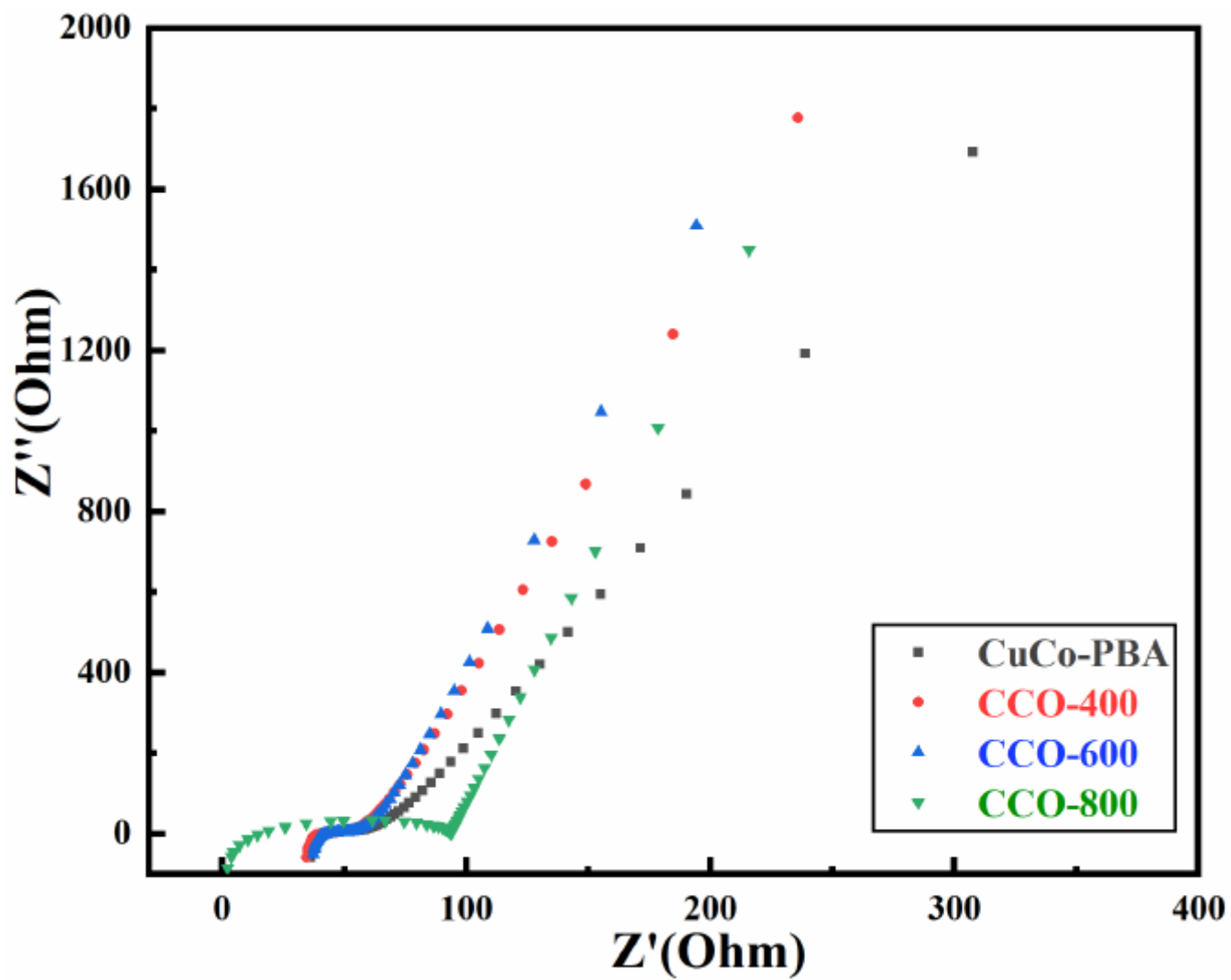


Figure 7

The Nyquist plots of EIS at 0.6 V of as-prepared catalysts.

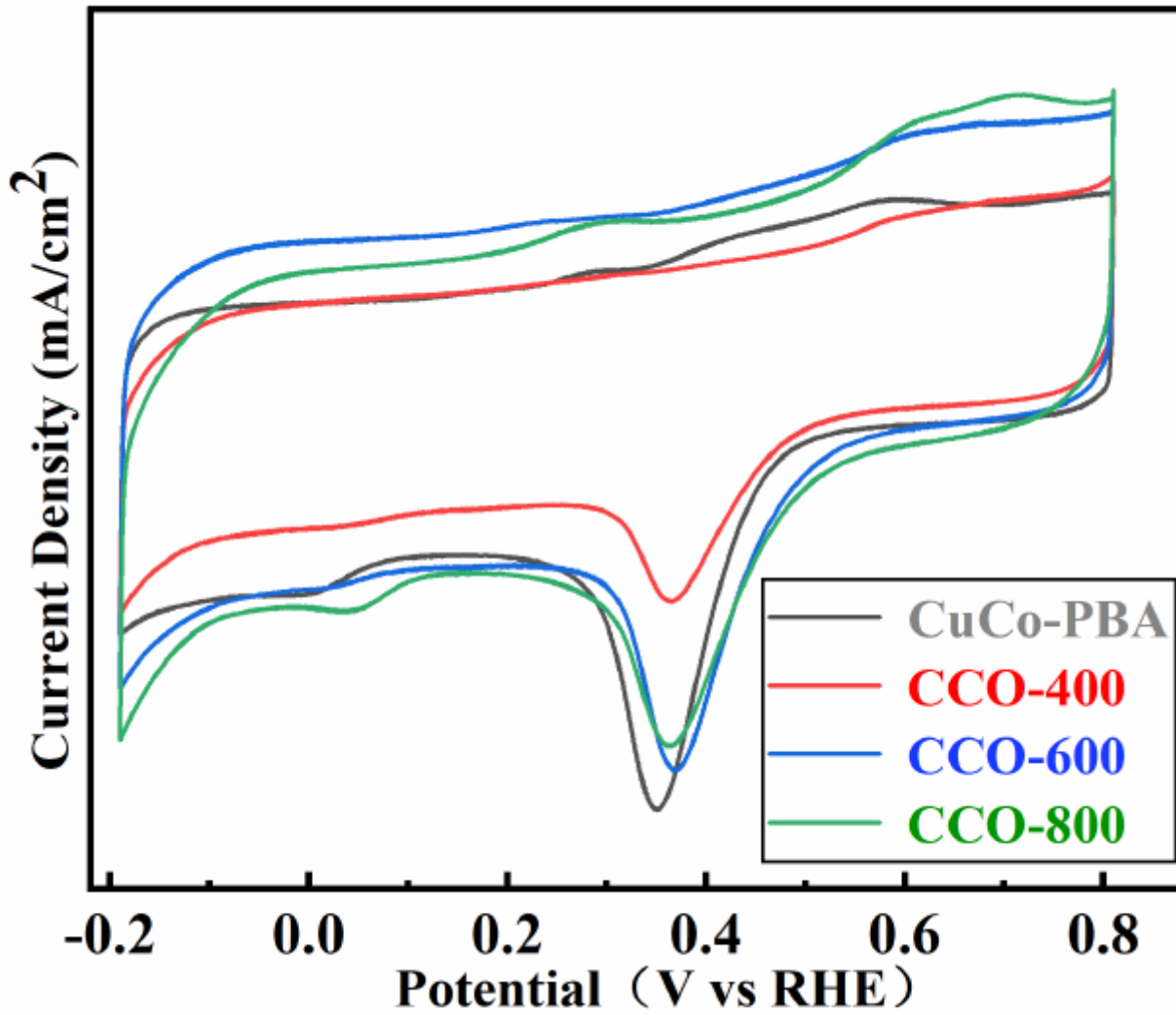


Figure 8

CV curves of the as-prepared catalysts in O₂ saturated 3.5 wt% NaCl.

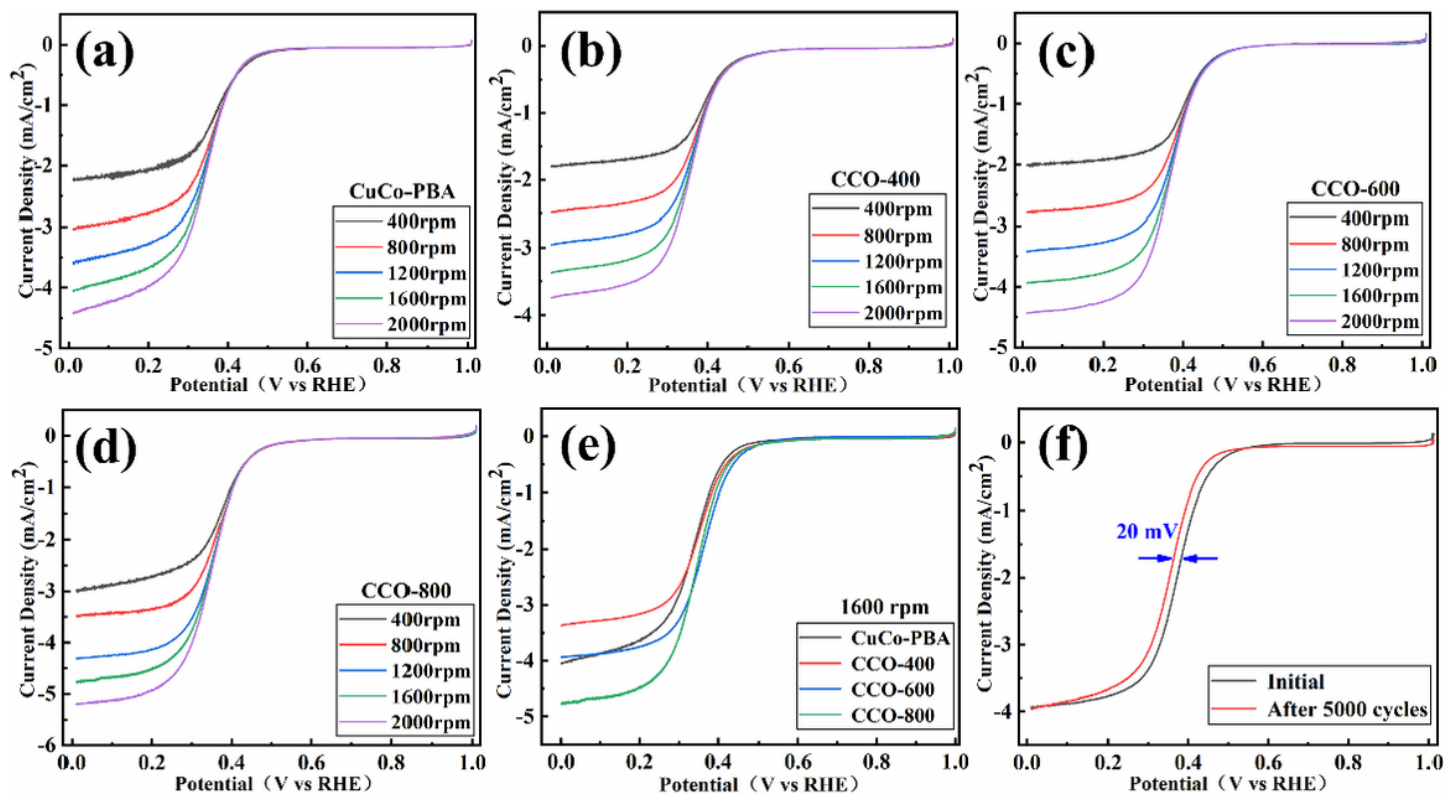


Figure 9

LSV curves of the (a) CuCo-PBA. (b) CCO-400. (c) CCO-600. (d) CCO-800. (e) LSV curves of various catalysts with a 1600 rpm rotate speed in O₂ saturated 3.5 wt% NaCl electrolyte. (f) LSV curves of the CCO-600 before and after 5000 cycles.

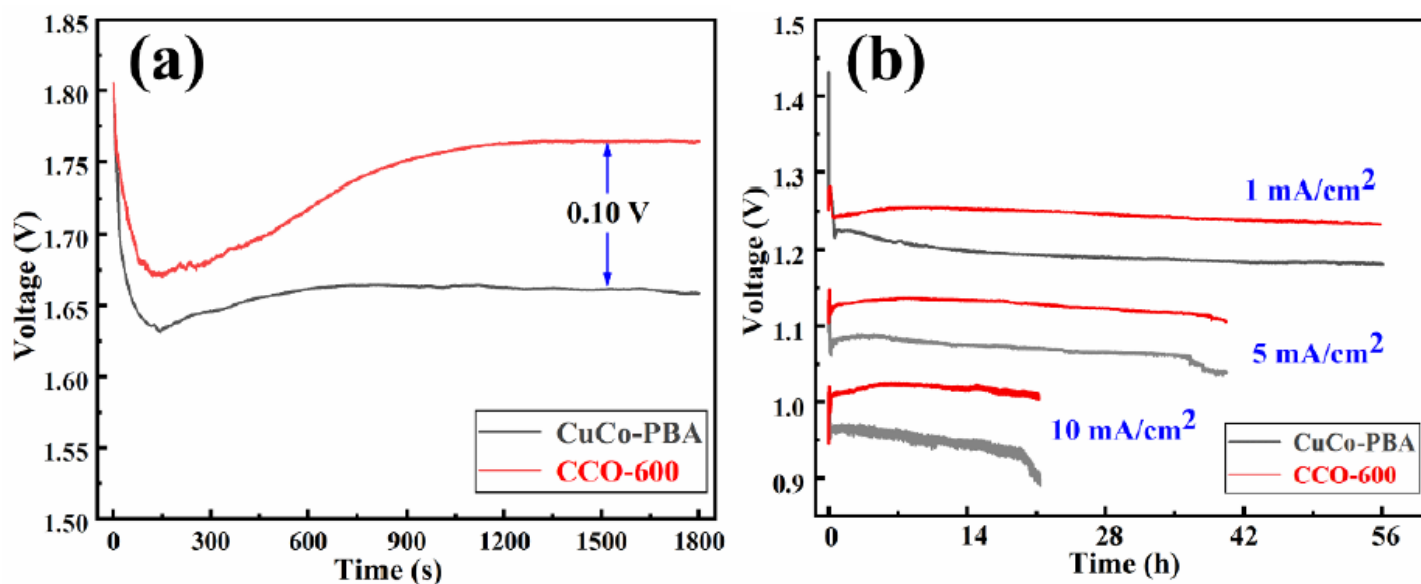


Figure 10

(a) The OCV of Mg-air batteries with different cathode catalysts. (b) The discharge performance of Mg-air batteries with different cathode catalysts at different current densities.